Rayleigh waves in locally resonant metamaterials

Rayleigh waves in locally resonant metamaterials

Farhad Zeighami[a,1], Antonio Palermo[a,1], Alessandro Marzani[a,*]

[a]*Department of Civil, Chemical, Environmental and Materials Engineering - DICAM, University of Bologna, 40136 Bologna, Italy*

Abstract

The design of metamaterials for surface waves control is an emerging field of research which can impact several technical applications, from electronic devices based on surface acoustic waves (SAW) to wave barriers for seismic isolation. So far, studies on the interaction of surface waves with locally resonant metamaterials have been limited to the context of metasurfaces, i.e., thin resonant interfaces or structures attached to the free surface of a waveguide.

In this work we remove this constraint by formulating an original dispersion relation for vertically polarized surface waves of the Rayleigh-type existing in resonant metamaterials. We consider the case of a resonant layer of thickness H coupled to a non-resonant half space. To easily account for the resonant material while setting the dispersion relation we propose a mixed dynamic-static homogenization approach, valid in the long wavelength regime. We show the existence of a band gap in the spectrum of the Rayleigh surface waves and relate its width to the region of negative effective density of the resonant metamaterial. We highlight how the thickness of the resonant layer affects the frequency stop-band and the magnitude of wave attenuation. We next derive and discuss the limit cases of a fully resonant half-space, i.e. a resonant layer with thickness $H >> \lambda$ where λ is the wavelength of the Rayleigh wave, and of the metasurface for small values of $H << \lambda$. In the latter case, we prove that our formulation properly model metasurfaces recovering previous formulations.

As case study, we analyse the propagation of seismic Rayleigh waves across a deep barrier of meter-size resonators embedded in the soil. The barrier is modeled using the proposed analytical approach. By means of high fidelity finite element simulations and Bloch analyses, we validate our novel findings including the homogenization approach and the derived dispersion relations.

Our work extends the knowledge on mechanical waves in metamaterials providing an analytical framework for the study of vertically polarized surface waves in resonant and partially resonant waveguides.

Keywords: Resonant metamaterial, Rayleigh waves, Band gap, Effective mass density, Effective moduli

1. Introduction

The term "Metamaterial" has emerged in recent years to indicate an artificial composite material that exhibits properties not commonly observed in natural materials. Introduced in optics around two decades ago [1, 2], metamaterials have later found their counterparts also in acoustics and mechanics [3, 4]. In mechanics, the so-called locally resonant metamaterials were initially conceived to filter and control the propagation of elastic bulk waves by exploiting the collective resonance of subwavelength inclusions embedded in a solid matrix [5]. Examples of this type of mechanical metamaterials can be realized by an arrangement of heavy solid inclusions coated with a layer of soft material and embedded in an elastic matrix [6]. This composite medium presents low-frequency band gaps around the inclusion resonance frequencies, which inhibit the propagation of elastic waves. The existence of band gaps is related to the manifestation of an "effective" negative mass density of the composite material around specific frequency bands.

Resonant induced band gaps can be found also in other elastic mechanical waveguides equipped with distributed resonators, like discrete mass-in-mass spring systems [7, 8, 9], trusses [10] and beams [11, 12, 13], resonant plates [14, 15, 16] and membranes [17], chiral lattices [18, 19] and architected 3D media [20, 21]. The description of the resonant units has been recently enriched to account for viscoelastic material behavior [22, 23, 24, 25], nonlinearity [26, 27, 28], hierarchical geometry [29, 30] and time-dependent mechanical properties [31, 32, 33].

When the resonant units are arranged at the free surface of an elastic waveguide, to form a so-called *metasurface*, the propagation of waves confined at the material surface can be controlled. For surface waves

*Corresponding author

Email address: alessandro.marzani@unibo.it (Alessandro Marzani)

[1]Equal contributors.

traveling in a half-space, examples of elastic metasurfaces comprise arrays of pillars or beams [34, 35, 36] and resonant inclusions [37] attached at or embedded close to the free surface of the half-space. Surface waves conversion [38, 39, 40], waveguiding [41], lensing [42, 43], rainbow trapping [44], tunable and uni-directional filtering [45, 46] are some of the unique dynamic effects obtained by using these metasurfaces. The above-mentioned effects can be predicted by deriving ad-hoc dispersion laws formulated by considering the metasurfaces as a boundary condition for the elastic waveguides.

Despite the numerous applications of metasurfaces, the scenarios where resonators are distributed through the whole medium depth or within a thick surface layer overlying a homogeneous half-space are still unexplored. Understanding the dynamics of these systems is fundamental to ease the development of novel devices to control and mitigate the propagation of surface waves, like barriers and foundations, recently conceived for ground vibrations and seismic waves [37, 47, 48].

Therefore, in this work we investigate the dynamics of surface waves of the Rayleigh-type propagating in a finite-thickness resonant layer overlying a homogeneous non-resonant half-space. The resonant layer consists in random distribution of discrete resonators in an elastic matrix. Such composite is modelled as an isotropic homogeneous material with effective mass density and elastic moduli able to replicate its dynamic response in the low-frequency regime. We use this description to derive an original dispersion relation which predicts the existence and extension of band gaps for vertically polarized surface waves.

As a case study, we apply our analytical framework to investigate the propagation of seismic waves through a deep barrier of resonators embedded in the soil, modelled as an equivalent resonant layer. In detail, we begin our investigation by considering the limit case of a resonant layer of depth much larger than the wavelength of interest, namely a resonant half-space. Next, we extend our study discussing the variation in dispersion properties and band gaps with respect to the resonant layer thickness. We verify the derived analytical dispersion relations by means of numerical simulations, exploiting finite element models (FEM), and Bloch's theorem [49]. Finally, numerical models are used to discuss the attenuation of Rayleigh-like waves propagating across a resonant layer of finite thickness and length.

The paper is organized as follows. In Sec. 2, we derive the dispersion relation of a finite-depth resonant layer laying over a homogeneous half-space. In Sec. 3 we investigate the dispersive properties of a seismic barrier, modelled by using the developed analytical framework. The results are validated against Finite Element (FE) simulations where the exact geometry of the resonant barrier is employed. In Sec. 4, harmonic analyses, performed via finite element simulations, are used to calculate the transmission coefficients of different resonant layer configurations and to compare their attenuation performances. Finally, some conclusions are drawn in Sec. 5.

2. Dispersion relation for vertically polarized surface waves propagating in a resonant layer coupled with a homogeneous non-resonant half-space

In what follows, we derive the dispersive properties of vertically polarized surface waves in a resonant layer of finite thickness H coupled to a homogeneous, isotropic, and elastic non-resonant half-space. Without loss of generality, we restrict our interest to waves propagating in the $x-z$ domain assuming plane-strain conditions.

2.1. Resonant layer and effective medium description

The resonant layer is composed of local resonators randomly distributed in the host medium (see Fig. 1). Each resonator consists of a rigid mass (m_r) suspended by horizontal and vertical springs with identical axial stiffness K. This yields to the existence of degenerate resonant modes with an angular frequency $\omega_{r,x} = \omega_{r,z} = \omega_r$ along the axes $x-z$. The local resonators have dimensions significantly smaller than the wavelength of the propagating surface waves (λ) in the low-frequency range of interest. Additionally, we assume the host material to be isotropic and homogeneous with Lamé parameters λ_h and μ_h and density ρ_h.

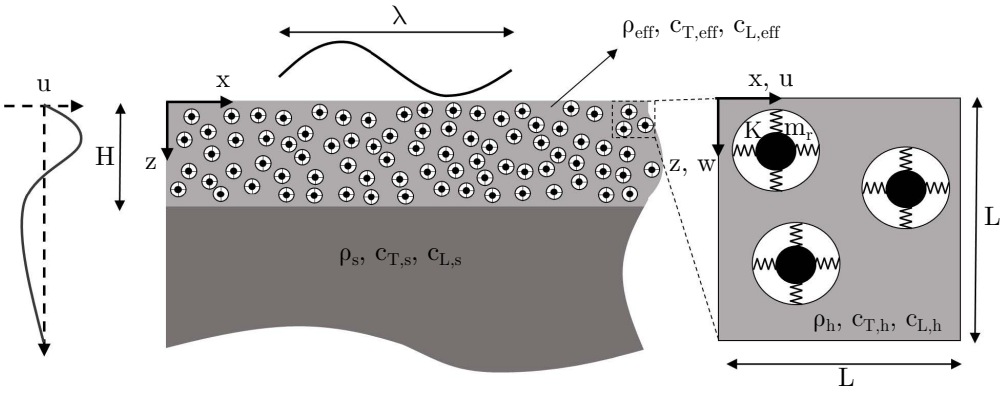

Figure 1: Schematic of a resonant layer made of randomly distributed resonators overlying a non-resonant homogeneous semi-infinite medium. The inset shows a detail of the reference volume element.

Under these assumptions, the dynamics of such resonant metamaterial can be appropriately described by means of an "effective" medium approach. The effective description aims at defining the properties of an equivalent homogeneous material with frequency-dependent mass density and bulk waves speeds able to approximate the dynamic response of the composite medium in the long-wavelength regime. Our purpose is to derive simple effective density and bulk speeds expressions for the resonant material and use them to obtain an analytical formulation of the dispersion laws for surface waves existing in the layered resonant medium. The analytical formulation should provide an accurate description of the low-frequency dynamics of the layered resonant medium.

For the definition of the effective density, we consider an ensemble of n discrete resonators embedded in the host material within a reference volume $V = St$, where $S = L^2$ is the surface area of the 2D plane-strain model (see inset in Fig. 1), and t is the unitary out-of-plane thickness. For this configuration, the effective density can be adequately represented by a scalar frequency-dependent function [50]:

$$\rho_{eff}(\omega) = \frac{m_h + nm_r}{V} + \frac{nm_r}{V}\frac{\omega^2}{\omega_r^2 - \omega^2} = \rho_0\left(1 + \alpha\frac{\omega^2}{\omega_r^2 - \omega^2}\right) \tag{1}$$

where ω is the angular frequency, m_h is the mass of host material enclosed in the reference volume, $\rho_0 = (m_h + nm_r)/V$ is the static ($\omega = 0$) density, and $\alpha = nm_r/(V\rho_0)$ is the ratio between the resonator mass per unit volume and the static density.

Given our interest in the low-frequency response of the resonant metamaterial, we resort to a static homogenization of its elastic parameters. Hence, for the definition of the effective elastic response of the composite material, here assumed to be isotropic at the length scale of interest, we need to compute two effective elastic parameters. For example, the reference volume material (or reference area in a 2D plane-strain model) can be subjected to a constrained uniaxial strain state (Fig. 2a) and to a shear strain state (Fig. 2b) to estimate the effective longitudinal modulus $M_{eff} = \lambda_{eff} + 2\mu_{eff}$ and the effective shear modulus μ_{eff}, respectively. If so, the two elastic parameters are calculated as:

$$M_{eff} = \frac{\overline{\sigma}_{xx}}{\overline{\varepsilon}_{xx}}, \quad \mu_{eff} = \frac{\overline{\sigma}_{xz}}{\overline{\gamma}_{xz}}, \tag{2}$$

where:

$$\overline{\sigma}_{xx} = \frac{\int_S \sigma_{xx} dS}{S}, \quad \overline{\varepsilon}_{xx} = \frac{\int_S \varepsilon_{xx} dS}{S}, \quad \overline{\sigma}_{xz} = \frac{\int_L \sigma_{xz} dL\, t}{Lt}, \quad \overline{\gamma}_{xz} = \frac{\Delta u}{L} \tag{3}$$

In Eq. (3), $\overline{\sigma}_{xx}$ and $\overline{\varepsilon}_{xx}$ are respectively the average stress and average strain components associated to the uniaxial constrained deformation state calculated within the host medium enclosed in the reference area S. Similarly, $\overline{\sigma}_{xz}$ and $\overline{\gamma}_{xz}$ are respectively the average shear stress calculated along the top surface of the reference volume element and the related average shear strain.

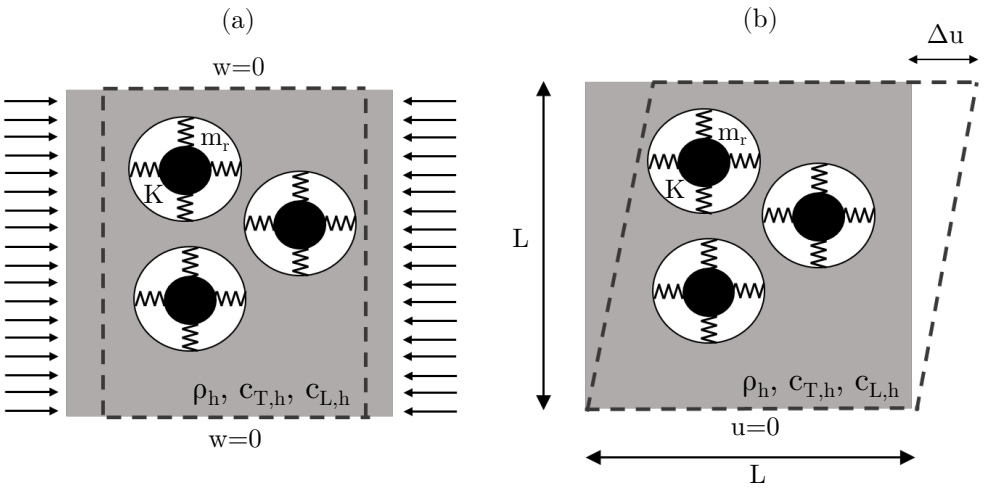

Figure 2: Schematics of the reference volumes used for the calculation of the (a) effective longitudinal modulus M_{eff} and (b) effective shear modulus μ_{eff}.

At this stage, the effective bulk velocities of the homogenized composite can be obtained as:

$$c_{L,eff}(\omega) = \sqrt{\frac{\lambda_{eff} + 2\mu_{eff}}{\rho_{eff}(\omega)}} \tag{4}$$

$$c_{T,eff}(\omega) = \sqrt{\frac{\mu_{e}ff}{\rho_{eff}(\omega)}} \tag{5}$$

These velocities are utilized in the analytical framework developed in the next section to describe the dispersive properties of surface waves in resonant materials.

2.2. Derivation of the dispersion relation

We now analyze the propagation of vertically polarized (Rayleigh-like) surface waves in a semi-infinite domain ($x - z$ plane, for $z > 0$), composed of a resonant layer of depth H overlying an elastic isotropic non-resonant half-space (see Fig. 1). The dynamics of the resonant layer is described by exploiting its frequency-dependent effective properties, namely ρ_{eff}, $c_{L,eff}$ and $c_{T,eff}$, as derived in Sec. 2.1, whereas the isotropic, homogeneous half-space is characterized by mass density ρ_s and longitudinal and shear waves speed $c_{L,s}$, and $c_{T,s}$, respectively.

We consider a plane harmonic wave propagating along the x-axis with a wavenumber k and angular frequency ω. For a wave polarized in the $x-z$ plane, the displacement vectors in the resonant layer $\boldsymbol{u}_1$ and the half-space $\boldsymbol{u}_2$ read:

$$\boldsymbol{u}_j = [u_j, v_j, w_j] \quad j = 1, 2 \tag{6}$$

where $v_1 = v_2 = 0$ are null displacement components. The displacement fields can be expressed in terms of the potential functions Φ_j, and $\Psi_{y,j}$:

$$u_j = \frac{\partial \Phi_j}{\partial x} - \frac{\partial \Psi_{y,j}}{\partial z}, \quad w_j = \frac{\partial \Phi_j}{\partial z} + \frac{\partial \Psi_{y,j}}{\partial x} \quad j = 1, 2 \tag{7}$$

where Φ_j is the scalar dilatation potential while $\Psi_{y,j}$ is the y-component of the distortional vector potential $\boldsymbol{\Psi}$. These potentials should satisfy the wave equations in both the resonant layer and the half-space:

$$\begin{aligned} \nabla^2\Phi_1 &= \frac{1}{(c_{L,eff})^2}\frac{\partial^2\Phi_1}{\partial t^2}, \quad \nabla^2\Psi_{y,1} = \frac{1}{(c_{T,eff})^2}\frac{\partial^2\Psi_{y,1}}{\partial t^2}, \\ \nabla^2\Phi_2 &= \frac{1}{(c_{L,s})^2}\frac{\partial^2\Phi_2}{\partial t^2}, \quad \nabla^2\Psi_{y,2} = \frac{1}{(c_{T,s})^2}\frac{\partial^2\Psi_{y,2}}{\partial t^2}. \end{aligned} \tag{8}$$

Solutions of Eqs. (8) can be provided in the form:

$$\begin{aligned}
\Phi_1(x,z,t) &= (a_1^d e^{ikr_1 z} + a_1^u e^{-ikr_1 z}) e^{i(\omega t - kx)}, \\
\Psi_{y,1}(x,z,t) &= (b_1^d e^{iks_1 z} + b_1^u e^{-iks_1 z}) e^{i(\omega t - kx)}, \\
\Phi_2(x,z,t) &= (a_2^d e^{ikr_2 (z-H)} + a_2^u e^{-ikr_2 (z-H)}) e^{i(\omega t - kx)}, \\
\Psi_{y,2}(x,z,t) &= (b_2^d e^{iks_2 (z-H)} + b_2^u e^{-iks_2 (z-H)}) e^{i(\omega t - kx)}.
\end{aligned} \tag{9}$$

where r_j and s_j, for $j = 1, 2$, are given by:

$$\begin{aligned}
r_1 &= \sqrt{\left(\frac{\omega}{k c_{L,eff}}\right)^2 - 1}, \quad s_1 = \sqrt{\left(\frac{\omega}{k c_{T,eff}}\right)^2 - 1}, \\
r_2 &= \sqrt{\left(\frac{\omega}{k c_{L,s}}\right)^2 - 1}, \quad s_2 = \sqrt{\left(\frac{\omega}{k c_{T,s}}\right)^2 - 1}.
\end{aligned} \tag{10}$$

and where a_j^d, b_j^d, a_j^u, and b_j^u, for $j = 1, 2$, denote the amplitudes of the downgoing (upperscript d) and upgoing (upperscript u) body waves, respectively. We restrict our interest to the derivation of surface wave solutions by assuming inhomogeneous potentials within the elastic half-space as:

$$\begin{aligned}
\Phi_2(x,z,t) &= a_2^d \, e^{-kr_2^*(z-H) + i(\omega t - kx)} \\
\Psi_{y,2}(x,z,t) &= b_2^d \, e^{-ks_2^*(z-H) + i(\omega t - kx)}
\end{aligned} \tag{11}$$

where:

$$r_2 = i r_2^*, \quad r_2^* = \sqrt{1 - \left(\frac{\omega}{k c_{L,s}}\right)^2}, \quad s_2 = i s_2^*, \quad s_2^* = \sqrt{1 - \left(\frac{\omega}{k c_{T,s}}\right)^2}, \tag{12}$$

and considering waves with phase velocity $c = \frac{\omega}{k} < c_{T,s} < c_{L,s}$. Note that the exponentially increasing waves in the half-space have been eliminated by imposing $a_2^u = 0$, and $b_2^u = 0$. Via simple algebraic manipulations, the potential functions in both the resonant and homogeneous half-space are rewritten as:

$$\begin{aligned}
\Phi_1(x,z,t) &= \Big(A_1 \cos(kr_1 z) + A_2 \sin(kr_1 z)\Big) e^{i(\omega t - kx)} \\
\Phi_2(x,z,t) &= A_3 \, e^{-kr_2^*(z-H) + i(\omega t - kx)} \\
\Psi_{y,1}(x,z,t) &= \Big(A_4 \cos(ks_1 z) + A_5 \sin(ks_1 z)\Big) e^{i(\omega t - kx)} \\
\Psi_{y,2}(x,z,t) &= A_6 \, e^{-ks_2^*(z-H) + i(\omega t - kx)}
\end{aligned} \tag{13}$$

where A_j, for $j = 1, ..., 6$, are constants which can be derived from a_j^u, a_j^d, b_j^u, b_j^d (e.g., $A_1 = a_1^d + a_1^u$). Substituting Eq. (13) into Eq. (7), and dropping the common propagating term $e^{i(\omega t - kx)}$, the horizontal and vertical displacement functions in the resonant layer can be derived as:

$$\begin{aligned}
u_1 &= -k\left[i\Big(A_1 \cos(kr_1 z) + A_2 \sin(kr_1 z)\Big) + s_1\Big(- A_4 \sin(ks_1 z) + A_5 \cos(ks_1 z)\Big)\right] \\
w_1 &= -k\left[r_1\Big(A_1 \sin(kr_1 z) - A_2 \cos(kr_1 z)\Big) + i\Big(A_4 \cos(ks_1 z) + A_5 \sin(ks_1 z)\Big)\right]
\end{aligned} \tag{14}$$

Similarly, the displacements in the half-space are obtained as:

$$\begin{aligned}
u_2 &= -k\Big(iA_3 \, e^{-kr_2^*(z-H)} - s_2^* A_6 \, e^{-ks_2^*(z-H)}\Big) \\
w_2 &= -k\Big(r_2^* A_3 \, e^{-kr_2^*(z-H)} + iA_6 \, e^{-ks_2^*(z-H)}\Big)
\end{aligned} \tag{15}$$

By exploiting linear elastic isotropic constitutive relations, the stress components within the layers are expressed

as:

$$\sigma_{zx,j} = \mu_j\left(\frac{\partial w_j}{\partial x} + \frac{\partial u_j}{\partial z}\right), \quad \sigma_{zz,j} = \lambda_j\, div\, \boldsymbol{u}_j + 2\mu_j \frac{\partial w_j}{\partial z}. \quad j = 1, 2. \tag{16}$$

We substitute the displacements of the layered systems, Eq. (14) and Eq. (15), into Eq. (16), to obtain the tangential and normal stresses in the resonant layer:

$$\begin{aligned}
\sigma_{zx,1} &= \rho_{eff}\omega^2\Big[ir_1\gamma_1\Big(A_1\ \sin(kr_1z) - A_2\ \cos(kr_1z)\Big) \\
&\quad - \delta_1\Big(A_4\ \cos(ks_1z) + A_5\ \sin(ks_1z)\Big)\Big], \\
\sigma_{zz,1} &= \rho_{eff}\omega^2\Big[\delta_1\Big(A_1\ \cos(kr_1z) + A_2\ \sin(kr_1z)\Big) \\
&\quad + i\gamma_1 s_1\Big(A_4\ \sin(ks_1z) - A_5\ \cos(ks_1z)\Big)\Big],
\end{aligned} \tag{17}$$

where, $\gamma_1 = 2\big(kc_{T,eff}/\omega\big)^2$ and $\delta_1 = \gamma_1 - 1$. Similarly, the stress components in the half-space are derived as:

$$\begin{aligned}
\sigma_{zx,2} &= \rho_s\omega^2\Big[ir_2^*\gamma_2 A_3\, e^{-kr_2^*(z-H)} - \delta_2 A_6\, e^{-ks_2^*(z-H)}\Big] \\
\sigma_{zz,2} &= \rho_s\omega^2\Big[\delta_2 A_3\, e^{-kr_2^*(z-H)} + \gamma_2 i s_2^* A_6\, e^{-ks_2^*(z-H)}\Big]
\end{aligned} \tag{18}$$

with, $\gamma_2 = 2\big(kc_{T,s}/\omega\big)^2$ and $\delta_2 = \gamma_2 - 1$.

At this stage, the governing boundary problem for the layered medium is obtained by imposing the following boundary conditions:

$$\sigma_{zx,1} = 0, \quad \sigma_{zz,1} = 0 \quad \text{for} \quad z = 0, \tag{19}$$

$$u_1 = u_2, \quad w_1 = w_2 \quad \text{for} \quad z = H, \tag{20}$$

$$\sigma_{zx,1} = \sigma_{zx,2}, \quad \sigma_{zz,1} = \sigma_{zz,2} \quad \text{for} \quad z = H. \tag{21}$$

namely, zero stresses at the medium free surface, Eq. (19), and continuity of displacements and stresses at the interface between the resonant layer and the half-space, Eq. (20), and Eq. (21), respectively. By exploiting the identities $A_2 = -A_4\delta_1/(ir_1\gamma_1)$ and $A_5 = A_1\delta_1/(is_1\gamma_1)$, we can reduce the boundary problem to a set of four independent equations. In particular, the continuity of displacements at the interface can be rewritten as:

$$\begin{aligned}
&i(cosP - \frac{\delta_1}{\gamma_1}cosQ)A_1 - (\frac{\delta_1}{r_1\gamma_1}sinP + s_1 sinQ)A_4 - iA_3 + {s_2}^* A_6 = 0 \\
&(r_1 sinP + \frac{\delta_1}{s_1\gamma_1}sinQ)A_1 + i(-\frac{\delta_1}{\gamma_1}cosP + cosQ)A_4 - {r_2}^* A_3 - iA_6 = 0
\end{aligned} \tag{22}$$

where $P = kr_1H$ and $Q = ks_1H$. Similarly, the equilibrium condition on the tangential and normal stresses at the interface can be reformulated as:

$$\begin{aligned}
&i(r_1\gamma_1 sinP + \frac{{\delta_1}^2}{s_1\gamma_1}sinQ)A_1 + \delta_1(cosP - cosQ)A_4 - \frac{\rho_s}{\rho_{eff}}\big(ir_2{}^*\gamma_2 A_3 - \delta_2 A_6\big) = 0 \\
&\delta_1(cosP - cosQ)A_1 + i(\frac{{\delta_1}^2}{r_1\gamma_1}sinP + s_1\gamma_1 sinQ)A_4 - \frac{\rho_s}{\rho_{eff}}\big(\delta_2 A_3 + is_2{}^*\gamma_2 A_6\big) = 0
\end{aligned} \tag{23}$$

The system of equations (22) and (23), can be rearranged in matrix form:

$$\begin{bmatrix}
i(cosP - \frac{\delta_1}{\gamma_1}cosQ) & -\frac{\delta_1}{r_1\gamma_1}sinP - s_1 sinQ & -i & {s_2}^* \\
r_1 sinP + \frac{\delta_1}{s_1\gamma_1}sinQ & i(-\frac{\delta_1}{\gamma_1}cosP + cosQ) & -{r_2}^* & -i \\
i\rho_{eff}(r_1\gamma_1 sinP + \frac{{\delta_1}^2}{s_1\gamma_1}sinQ) & \rho_{eff}\delta_1(cosP - cosQ) & -i\rho_s\gamma_2 {r_2}^* & \rho_s\delta_2 \\
\rho_{eff}\delta_1(cosP - cosQ) & i\rho_{eff}(\frac{{\delta_1}^2}{r_1\gamma_1}sinP + s_1\gamma_1 sinQ) & -\rho_s\delta_2 & -\rho_s i\gamma_2 {s_2}^*
\end{bmatrix}
\begin{bmatrix} A_1 \\ A_4 \\ A_3 \\ A_6 \end{bmatrix} =
\begin{bmatrix} 0 \\ 0 \\ 0 \\ 0 \end{bmatrix} \tag{24}$$

which can be written in a compact fashion as $\mathbf{D}(k,\omega)\mathbf{A} = \mathbf{0}$.

Non-trivial solutions of Eq. (24) are found by imposing the $\det(\mathbf{D}(k,\omega)) = 0$. Solutions of such nonlinear equation in the variables ω and k provide the dispersive properties of surface waves propagating in the layered

resonant medium.

2.3. Limit case: Dispersion relation of a full resonant half-space

Let us consider a configuration where the resonant layer extends along the whole depth of the medium, namely the case of a resonant half-space. For this configuration, it is necessary to specify only the potential functions in the resonant layer. As in the previous derivation, we restrict our search to wave solutions confined to the surface by assuming potentials with the form:

$$\begin{aligned}\Phi_1(x,z,t) &= a_1 e^{ikr_1^* z} e^{i(\omega t - kx)},\\ \Psi_{y,1}(x,z,t) &= b_1 e^{iks_1^* z} e^{i(\omega t - kx)}\end{aligned} \tag{25}$$

where:

$$r_1^* = \sqrt{\left(1 - \frac{\omega}{kc_{L,eff}}\right)^2}, \quad s_1^* = \sqrt{\left(1 - \frac{\omega}{kc_{T,eff}}\right)^2} \tag{26}$$

The dispersion relation of a resonant half-space can be obtained by expressing the stress components in the resonant medium, Eqs. (16), as functions of the potentials in Eqs. (25) and imposing the free-stress boundary conditions at the surface of the half-space, Eq. (19). The procedure yields a system of two homogeneous equations:

$$\begin{bmatrix} -2i\sqrt{1-\left(\frac{\omega}{kc_{L,eff}}\right)^2} & 2-\left(\frac{\omega}{kc_{T,eff}}\right)^2 \\ \left(\frac{\omega}{kc_{T,eff}}\right)^2 - 2 & -2i\sqrt{1-\left(\frac{\omega}{kc_{T,eff}}\right)^2} \end{bmatrix} \begin{bmatrix} a_1 \\ b_1 \end{bmatrix} = \begin{bmatrix} 0 \\ 0 \end{bmatrix}. \tag{27}$$

Non-trivial solutions of Eq. (27) provide the dispersion law for Rayleigh waves in a resonant half-space:

$$\left(2 - \left(\frac{\omega}{kc_{T,eff}}\right)^2\right)^2 - 4\sqrt{1-\left(\frac{\omega}{kc_{T,eff}}\right)^2}\sqrt{1-\left(\frac{\omega}{kc_{L,eff}}\right)^2} = 0. \tag{28}$$

Note that Eq. (28) has the same form of the classical expression of Rayleigh waves in a homogeneous medium [51], here adapted with the "effective" velocities of the elastic half-space.

In the following section, we utilize the obtained analytical formulation in Eqs. (24) and (28) to evaluate and discuss the dispersive properties of surface waves propagating through resonant layers with different thicknesses.

3. Case study: Dispersive properties of seismic barriers

To validate our analytical framework and discuss the fundamental dispersive features of surface waves in resonant materials, we consider the scenario of an array of meter-size resonators, known as metabarrier [37], embedded in the soil to attenuate the propagation of seismic surface waves and ground vibrations. The validation of our approach, which comprises the effective medium description and the related dispersion relations, is performed by comparing the predictions of the analytical models with the numerical outcomes of finite element models, where the resonant unit cells are modeled accounting for their exact geometries and mechanical parameters.

The configuration of interest is displayed in Fig. 3a. It comprises a layer of resonators embedded in the soil and arranged periodically in a square lattice of spacing a, for an overall depth H. Each unit cell consists in a resonator attached to the host medium via elastic connectors, modelled as discrete springs, with identical horizontal and vertical stiffness K, as schematically shown in Fig. 3b. For our numerical calculations we consider a unit cell (see Fig. 3b) with length $a = 1$ [m], with a square hole of length $a_v = 0.6\,a$ enclosing a resonator of dimensions $a_r \times a_r = 0.25\,a^2$. The host medium is a soft soil with mass density $\rho_h = 1500$ $[kg/m^3]$, and bulk longitudinal and shear velocities of $c_{L,h} = 335$ [m/s], and $c_{T,h} = 120$ [m/s] [37], respectively. The 2D plane-strain model has an out-of-plane thickness $t = 1$ [m]. The mass of the resonator is $m_r = \rho_r a_r^2 t$, where $\rho_r = 2400$ $[kg/m^3]$ is the mass density, and $\omega_r = 2\pi f_r$ is the angular resonant frequency of the resonator, with $f_r = 5$ Hz.

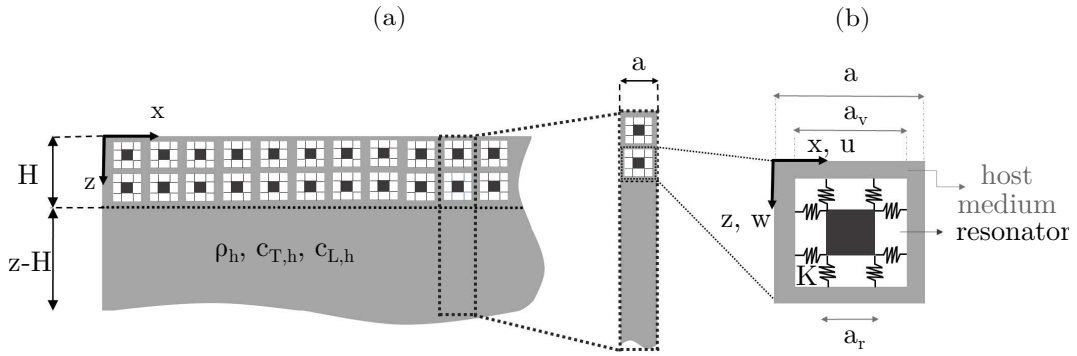

Figure 3: (a) Schematics of the resonant layer with a regular grid of embedded resonators overlying a homogeneous half-space. In the inset is shown a representative strip of the bilayered half-space. (b) Barrier unit cell.

In accordance with the assumptions of the analytical model (Sec. 2), we restrict our analysis to the low-frequency range where the dimensions of the resonators are much smaller than both the wavelength and the penetration depth of the fundamental surface mode. In this scenario, the density of the resonant unit can be adequately described using the approach discussed in Sec. 2. Similarly, we approximate the elastic response of the composite material as an effective isotropic medium. In doing so, we neglect the orthotropic behaviour induced by the square lattice arrangement of the resonators. Still, we demonstrate that this approach can capture the fundamental physics of the considered problem.

3.1. Effective resonant layer model of the seismic barrier

To characterize the elastic properties (M_{eff} and μ_{eff}) of the unit cell, we utilize the procedure discussed in Sec. 2. The calculation of the average stresses is performed via FE simulations using the software Comsol Multiphysics [52]. In more detail, we model a unit cell of the barrier under plane-strain conditions using Lagrange quadrilateral elements to discretize the host material and truss elements for the springs connecting the host material to the resonator. For the calculation of the longitudinal modulus, we impose a unitary lateral pressure load to the unit cell restraining its top and bottom boundaries along the vertical direction (see Fig. 4a). Fig. 4c and Fig. 4e depict the obtained longitudinal stress and strain distributions obtained, respectively. We calculate the average stress $\overline{\sigma}_{xx}$ and strain $\overline{\varepsilon}_{xx}$ components within the host medium, and estimate an effective longitudinal modulus $M_{eff} = \overline{\sigma}_{xx}/\overline{\epsilon}_{xx} = 36.37$ [MPa].

For the calculation of the shear modulus μ_{eff} we impose a unitary horizontal displacement at the top surface of the unit cell, restraining the bottom boundary along the horizontal direction (Fig. 4b). Additionally, we impose continuity conditions along the unit cell lateral boundaries to simulate the effect of neighboring unit cells. Fig. 4d and Fig. 4f show the obtained shear stress and strain distributions, respectively. From the average stress $\overline{\sigma}_{xz}$ we estimate an effective shear modulus $\mu_{eff} = \overline{\sigma}_{xz}/\overline{\gamma}_{xz} = 3.66$ [MPa].

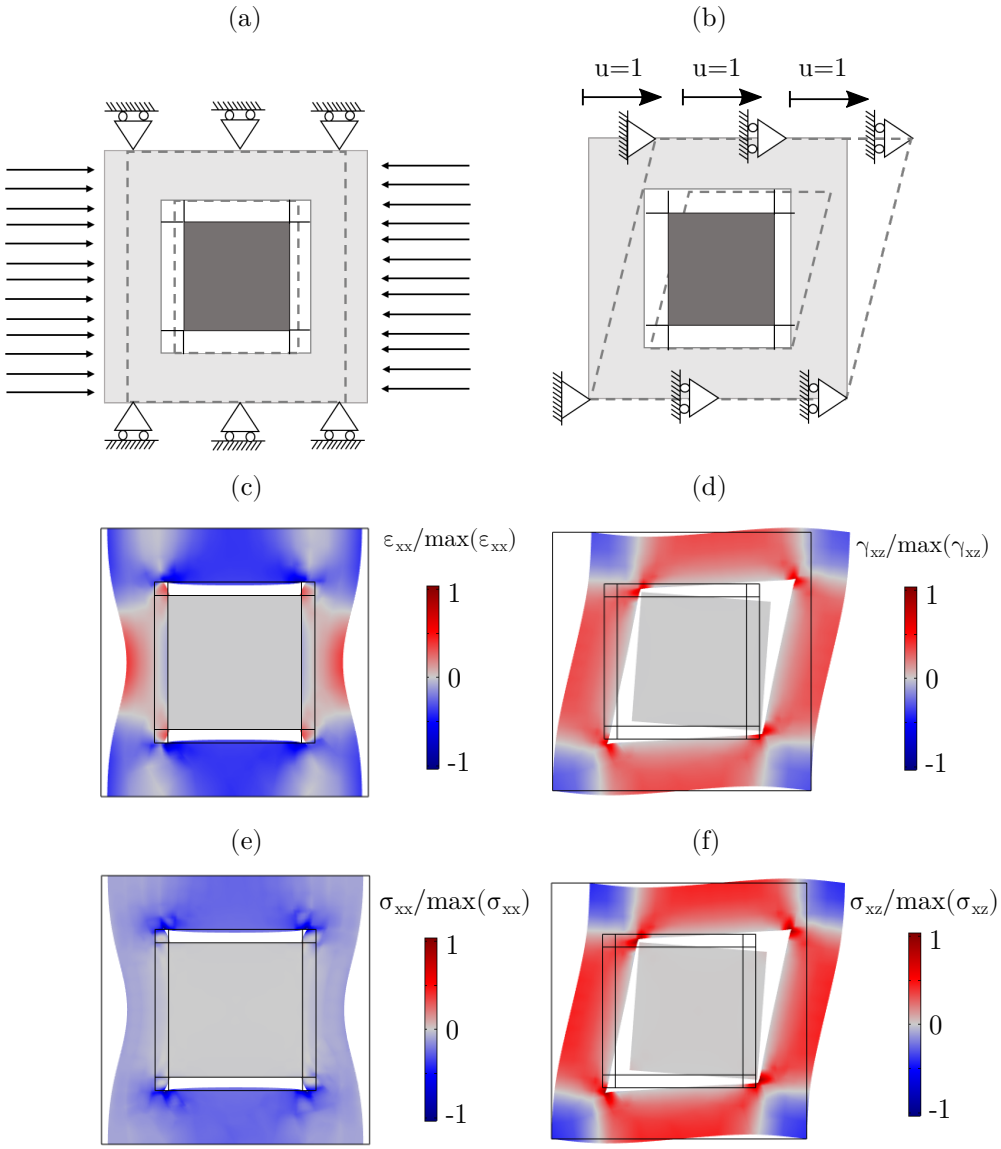

Figure 4: (a) Schematics of the FE model used to calculate the longitudinal modulus M_{eff}, and (b) shear modulus μ_{eff} of the resonant barrier. Longitudinal strain (c) and stress (e) components associated with the uniaxial constrained deformation state. Shear strain (d) and stress (f) components associated with the pure shear deformation state.

For the calculation of the unit cell effective mass density (EMD) we utilize Eq. (1). Given the regular arrangement of the resonators, we consider as reference volume the one of a unit cell which encloses a single resonator, i.e., $V = a^2 t = 1\,[\mathrm{m}^3]$ and $n = 1$ in Eq. (1). As a result, the static density of the homogenized medium is $\rho_0 = (m_h + m_r)/V = 1560$ [kg] with $m_h = \rho_h(a^2 - a_v^2)t = 960$ [kg] being the mass of the external host medium enclosed in a unit cell; whereas the mass ratio $\alpha = m_r/(V\rho_0) = 0.384$.

The value of the effective density calculated as per Eq. (1) is reported in Fig. 5a in terms of normalized density $\rho' = \rho_{eff}/\rho_0$ and normalized angular frequency $\omega^{'} = \omega/\omega_r$. As shown in literature, the effective density assumes negative values in the interval $\omega^{'} \in [1, (1/(1-\alpha))^{1/2}]$ due to the out-of-phase motion between the internal oscillator and the host medium. Conversely, in the long-wavelength (low-frequency) limit, the density recovers its static value $\rho_{eff}(\omega = 0) = \rho_0$, while in the high frequency limit it approaches $\rho_{eff}(\omega = \infty) = m_h/V$, namely the resonator mass does not contribute to the unit cell effective inertia.

Knowledge of the effective density and effective longitudinal and shear moduli allow us calculating the bulk velocities of the resonant layer to approximate the dynamics of the seismic barrier in the low-frequency range. In Fig. 5b, the values of the bulk velocities, which are normalized by the shear velocity of host medium $c_{T,h}$, are reported in the normalized frequency range $\omega' = [0, \quad 3]$. As expected, in the frequency range where the effective mass density of the cell assumes negative values, the effective bulk velocities have null real components (Fig. 5b) and non-null imaginary values with an asymmetric profile (Fig. 5c) characteristic of a resonant type frequency band gap (BG). Note that the BG of both the bulk modes occurs within the same frequency region due to the isotropic behavior of the resonators.

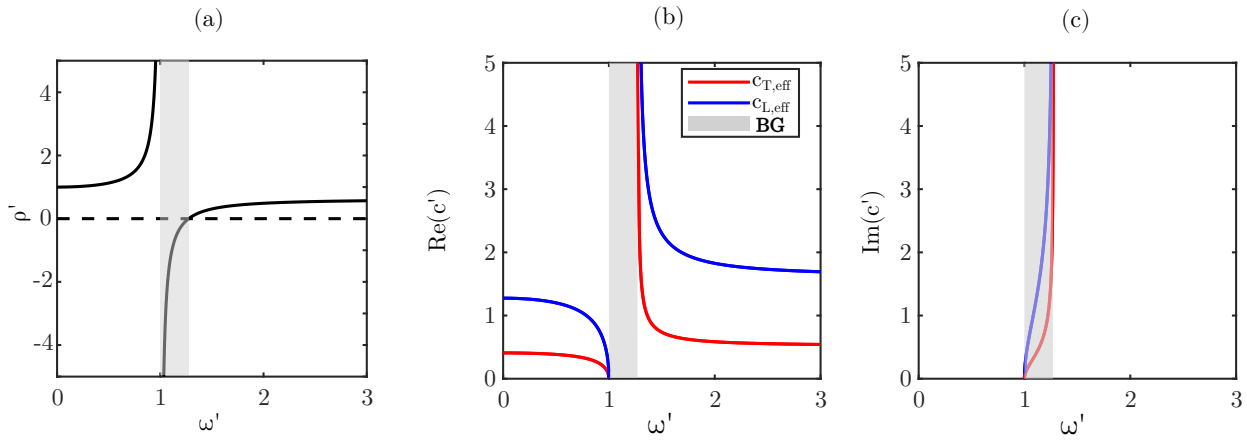

Figure 5: Effective properties of the resonant barrier. (a) Effective mass density. (b) Effective velocities of propagating bulk waves and (c) evanescent bulk waves. Shaded areas indicate the band gap associated with negative EMD and purely imaginary values of the effective velocities.

3.2. Dispersive properties of a deep seismic barrier modelled as a resonant half-space

We start our investigation considering a configuration where the depth of the barrier, namely the depth of the resonant layer, has a thickness $H >> \lambda$. For this scenario, we can neglect the presence of the homogeneous substrate and exploit the analytical relation derived for the case of a resonant half-space, Eq. (28), to predict the dispersive properties of Rayleigh-like waves.

In particular, we seek for the complex wavenumbers $k = \Re(k) + i\Im(k)$ of Eq. (28) in the dimensionless angular frequency range ω'=[0, 2.5], where the resonance modes of the unit cell should be found. The real $\Re(k')$ vs. ω' and imaginary $\Im(k')$ vs. ω' dispersion curves, calculated using a bisection root-finding scheme, are shown in Fig. 6a, and Fig. 6b, respectively, by continuous black lines. The black dashed line in Fig. 6a denotes the non-dispersive roots of the Rayleigh wave solutions in the homogeneous soil (hosting medium).

We observe that the resonant half-space is characterized by a BG for the surface waves in the frequency range where the EMD is negative. This result can be interpreted by recalling that a Rayleigh wave stems from the interaction between the bulk longitudinal and shear waves. Hence, in the frequency range where bulk waves are impeded by the resonant metamaterial, the Rayleigh solutions cannot propagate too.

Additionally, we observe that the Rayleigh mode in the resonant medium decay with an attenuation, i.e., $\Im(k_{R,eff})$, that is comparable to the one of a shear wave ($\Im(k_{T,eff})$) and greater than the one of the longitudinal bulk mode ($\Im(k_{L,eff})$), see Fig. 6b. This occurs because the imaginary component of the wavenumber is inversely proportional to the imaginary component of the velocity, namely $\Im(k) = \frac{\omega}{\Im(c)}$. Thus, the ratio $\frac{\Im(k_{R,eff})}{\Im(k_{L,eff})}$ is equal to the ratio of the velocities $\frac{\Im(c_{L,eff})}{\Im(c_{R,eff})}$ (compare Fig. 5b to Fig. 6d). Interestingly, the ratio of the velocities do not vary within the gap and is equal to the ratio of the real components $\frac{\Re(c_{L,eff})}{\Re(c_{R,eff})}$, calculated at any frequency outside the gap (compare Fig. 6c to Fig. 5a). Since the latter ratio is always larger than 1 for any material, the same result applies to the ratio $\frac{\Im(k_{R,eff})}{\Im(k_{L,eff})}$. Similar arguments apply to the comparison between Rayleigh and shear waves.

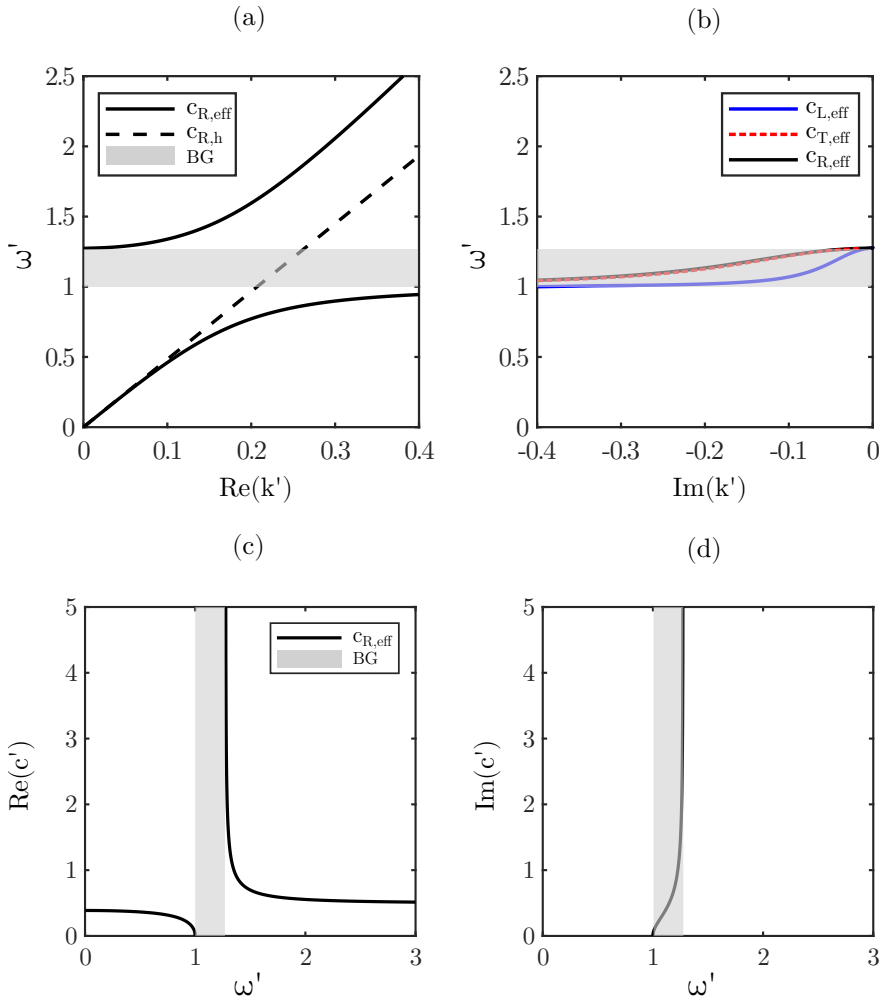

Figure 6: (a) Real and (b) imaginary wavenumber for the dispersion of Rayleigh waves propagating across a full resonant half-space, respectively. (c) Real and (d) imaginary parts of the effective Rayleigh wave velocity in the resonant medium, respectively.

3.2.1. Rayleigh-like mode shapes in the resonant half-space

We now exploit the effective medium description to reconstruct the Rayleigh-like mode shapes within the resonant half-space as [51]:

$$\begin{aligned} u_r &= -ikB_1 e^{-\eta z} + B_2 \zeta e^{-\zeta z} \\ w_r &= -\eta B_1 e^{-\eta z} - ikB_2 e^{-\zeta z} \end{aligned} \tag{29}$$

where u_r and w_r are the amplitudes of the horizontal and vertical components of the eigenmode, respectively, $\eta = (k^2 - (\omega/c_{L,eff})^2)^{(1/2)}$, $\zeta = (k^2 - (\omega/c_{T,eff})^2)^{(1/2)}$, and z is the coordinate depth of the resonant half-space. The constants B_1 and B_2 are arbitrarily chosen to satisfy Eq. (29), for example $B_2 = 1$ and $B_1 = (-2i\zeta k)/(\zeta^2 + k^2)$.

Examples of Rayleigh-like mode shapes propagating within the resonant half-space at the normalized frequency $\omega' = 0.8$ and $\omega' = 1.5$ corresponding to the in-phase (lower) and the out-of-phase (upper) dispersive branches are shown in Fig. 7a and 7b, respectively. The reader can compare these eigenshapes with those of the Rayleigh wave propagating in the homogeneous host medium (u_h,w_h), i.e., soil with no resonators (dashed lines in Fig. 7). The displacements are normalized by their corresponding absolute value at $z = 0$ and are represented along the normalized depth coordinate z/λ_0, where $\lambda_0 = 2\pi c_{R,h}/\omega_r$, and $c_{R,h} = 113.5$ [m/s] denotes the Rayleigh velocity of the host material. Comparison between Rayleigh modes in the resonant and non-resonant half-spaces propagating at a frequency slightly lower than the BG, reveals that the mode is more confined to the surface due to the lower effective velocity. In analogy, modes above the band gap are less confined due to the larger effective velocity.

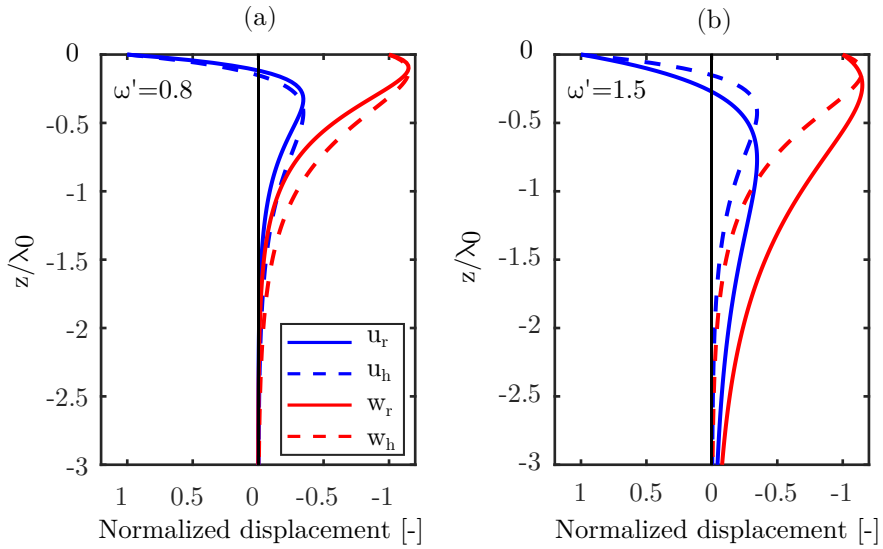

Figure 7: Rayleigh wave mode shapes in resonant half-space (continuous lines) and in the host medium (dashed lines) computed for a dimensionless circular frequency of (a) $\omega' = 0.8$ (in-phase), and (b) $\omega' = 1.5$ (out-of-phase).

3.2.2. FE Validation

To verify the analytical predictions provided by the proposed effective medium approach, we develop a bi-dimensional Finite Element (FE) model to compute the roots of the dispersion relation. To this aim, we model a representative strip of the resonant half-space in plane-strain condition, with a depth of $3\lambda_0$ and a width equal to that of the resonant unit cell $a << \lambda_0$, as shown in Fig. 8a. The depth of the strip is adequate to simulate a half-space domain in the frequency range around the unit cell resonance.

The base displacement of the strip in Fig. 8a is restricted both horizontally and vertically to prevent any undesirable rigid motion. Bloch boundary conditions are applied along the side edges of the model to replicate the dynamics of an infinite half-space in the x-direction. To accurately model the shortest wavelength at the highest frequency of interest, the domain is discretized by Lagrange quadrilateral elements with a minimum and maximum dimensions of $d_{min} = a/10$ and $d_{max} = a/5$, respectively.

The eigensolutions of the FE problem for given real wavenumbers from zero to $k' = 0.4$ are marked by dots in Fig. 8b, whereas our analytical solutions of Eq. (28) are reported in continuous black lines. The numerical model predicts a plethora of solutions that include several bulk-like modes. To discriminate between surface solutions and the bulk modes, we use a selection criterion based on the position of the displacement shape centroid G_r within the strip depth:

$$G_r = \frac{\int_0^{3\lambda_0} |w| z \, dz}{\int_0^{3\lambda_0} |w| \, dz} < 0.9\lambda_0 \tag{30}$$

thus selecting only those modes with a displacement centroid located within the uppermost region of the model depth. The analytical predictions well match the surface modes selected according to this criterion, which are marked by blue dots in Fig. 8b. In addition, the numerical model predicts a flat branch of eigensolutions at $\omega' = 1.72$, resulting from the rotational motion of the resonators (see detail in Fig. 8d).

We now analyze some of the mode shapes obtained from the numerical model. For better visualization, we display the wave field by replicating the eigenmode of the unit cell with a phase shift e^{ikx} along the direction of wave propagation. The surface mode with angular frequency $\omega^{'} = 0.91$, and wavenumber $k^{'} = 0.3$ is shown in Fig. 8e. We note that each resonator moves in-phase with the motion of the host medium (the colour in Fig. 8e denotes the w displacement amplitude), as observed along the acoustic branch of any resonant waveguide. Conversely, the wave field at $\omega^{'} = 2.11$ and $k^{'} = 0.3$ is characterized by an out-of-phase motion between the resonator and the hosting medium, which is typical of the optical branch of resonant materials (see Fig. 8c).

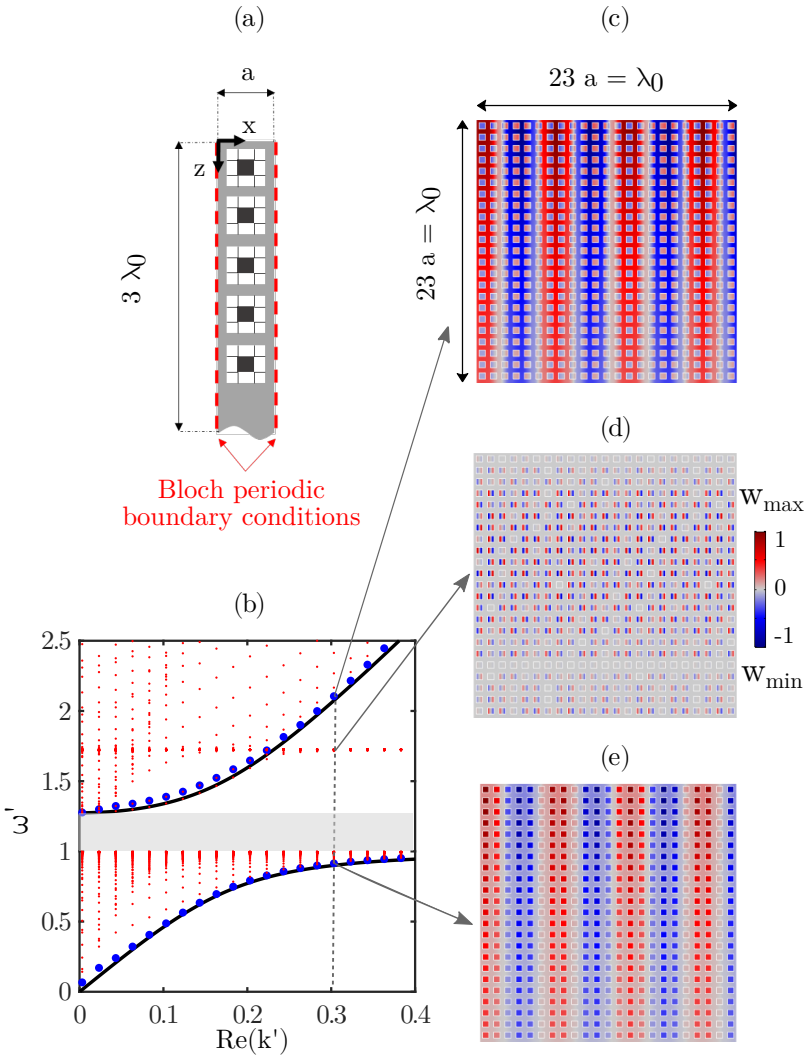

Figure 8: (a) Schematic of a strip of the resonant half-space. (b) Dispersion relation of the resonant half-space. Solid lines present the analytical solutions, and circles mark the FE eigensolutions (blue dots denote the surface modes). (c) Zoom-in on the wave field ($H = \lambda_0$) of a surface mode computed at $\omega^{'} = 2.11$ and $k^{'} = 0.3$ showing an out-of-phase displacement between the internal mass and the host medium; (d) rotating mode at $\omega^{'} = 1.72$ and $k^{'} = 0.3$; (e) surface mode computed at $\omega^{'} = 0.91$ and $k^{'} = 0.3$ with in-phase motion between the host medium and the internal resonant mass.

3.3. Dispersion of finite-depth seismic barriers

We now generalize our investigation by calculating and discussing the dispersive properties of Rayleigh-like waves traveling in a seismic barrier of depth H, modelled as a resonant layer of the same depth, overlaying a half-space of homogeneous soil. Our aim is to find the roots of $\det(\mathbf{D}(k,\omega)) = 0$, calculated as per Eq. (24), within the frequency range where we expect to observe the surface wave band gap. To this purpose, we calculate the determinant within the frequency range $\omega^{'} = [0, 2.5]$ and wavenumber range $k^{'} = [0, 0.5]$, and visualize its minimal values in Fig. 9a for a resonant layer of depth $H = \lambda_0$. Note that this depth corresponds roughly to a barrier of 23 unit cells.

Differently from the resonant half-space scenario, the bilayer medium supports the propagation of multiple surface modes (marked by blue lines in Fig. 9a). These surface waves are hybridized by the unit cell resonant modes. The hybridization leads to the generation of a low-frequency resonant band gap, bounded between the resonance frequency of the barrier ω_r and the crossing point between the bulk shear velocity $c_{T,h}$ of the half-space and fundamental hybridized mode, marked as a continuous black line in Fig. 9a.

The half-space shear velocity identifies the $\omega^{'}$-$k^{'}$ domain, labelled as sound-cone and highlighted by a dark gray area in Fig. 9a, where purely surface-confined modes cannot exist because s_2^* in Eq. (12) assumes imaginary values. Inside this domain we should instead observe leaky surface modes, which radiate part of their energy into the half-space. For example, by tracking the fundamental mode, i.e., by solving $\det(\mathbf{D}(k,\omega)) = 0$ numerically for the unknown complex wavenumbers $k = \Re(k) + i\Im(k)$, we can verify that a branch of this mode extends within the sound-cone. Additionally, we observe that the same mode becomes evanescent $\Re(k) = 0$, and $\Im(k) \neq 0$, within the frequency BG of the bulk modes, where both r_1 and s_1 in Eq. (10) assume imaginary values (see Fig. 9b).

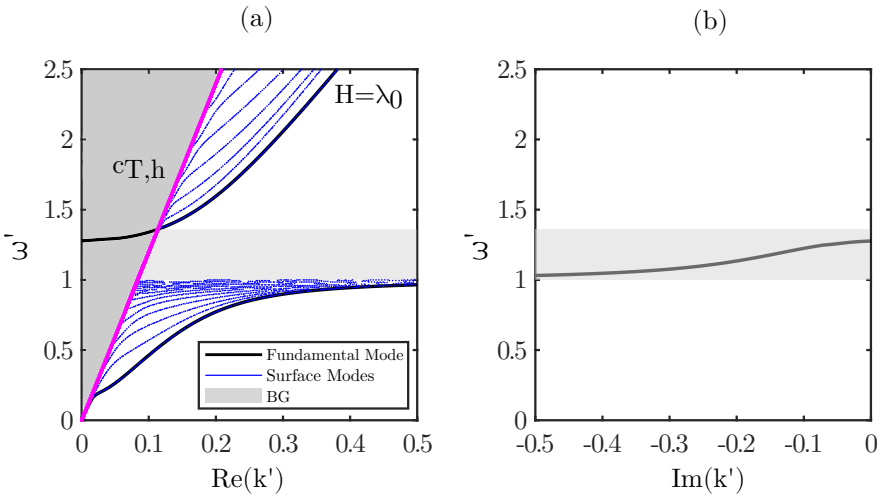

Figure 9: Dispersion relation of (a) propagating and (b) evanescent surface waves in a resonant layer with a depth of $H = \lambda_0$ overlaying a homogeneous half-space. The fundamental surface mode is marked by black lines.

We extend our investigation considering configurations with different resonant layer depths, $H = [0.2, 0.5, 1, 2]\lambda_0$, with $H = 0.2\lambda_0$ roughly corresponding to a barrier of five unit cells and $H = 2\lambda_0$ corresponding to a barrier of 46 unit cells along the depth of the resonant layer, respectively. The related real dispersive properties are shown in Figs. 10(a)-(d). A comparison between the analyzed scenarios shows that an increase in the thickness of the resonant layer widens the frequency range of the BG. To quantify this behavior, we calculate the BG extension for different depths of the resonant layer by visually inspecting the crossing point of fundamental surface mode and shear velocity of half-space.

The band gap evolution in terms of normalized angular frequency is shown in Fig. 10e for the normalized variation depth (H/λ_0) of the resonant layer. We observe a linear trend for resonant layers with $H < 0.5\lambda_0$. The BG extension reaches a maximum value $\omega^{'}_{RL} = 1.37$ for $H \geq 0.5\lambda_0$, which is larger than the band gap of a resonant half-space, whose upper edge $\omega^{'}_{HS}$ is indicated in Fig. 6a. The latter result can be interpreted by recalling that in the resonant layered system two attenuation mechanisms contribute to prevent the propagation of surface waves. First, as in the case of a fully resonant half-space, the bulk modes within the resonant layer are impeded within the frequency range where the effective density assumes negative values. As a result, the surface modes which stem from the superposition of these bulk modes (see Eq. (9)) are inhibited. Second, within an additional frequency range above the bulk waves BG, the apparent phase velocity of the surface modes assumes values $c > c_{T_h}$. This condition allows only the existence of leaky modes that disperse their energy in the half-space region, as discussed for the barrier with $H = \lambda_0$.

Regarding the case of a thin resonant layer, we underline that its dispersive properties can be equally predicted by treating the presence of the resonators as a stress boundary condition on the half-space (see Appendix A). This description, widely employed in literature to describe the dynamics of metasurfaces, yields a closed-form estimation of the upper edge frequency of the BG [37]:

$$\omega^{'}_{MS} = \beta + \sqrt{\beta^2 + 1}, \tag{31}$$

where:

$$\beta = \frac{m_{res}\ \omega_r}{2a_{res}\ \rho_h\ c_{T,h}} \sqrt{1 - \left(\frac{c_{T,h}}{c_{L,h}}\right)^2}. \tag{32}$$

The reader can appreciate that this prediction, marked by a red dashed line in Fig. 10e, well matches the BG extension of a thin $H = 0.05\lambda_0$ resonant layer, i.e., approximately a single unit cell layer, calculated according to our framework.

3.3.1. FE Validation

To verify the dispersion results found analytically, we develop a dedicated finite element numerical model, and perform numerical simulations.

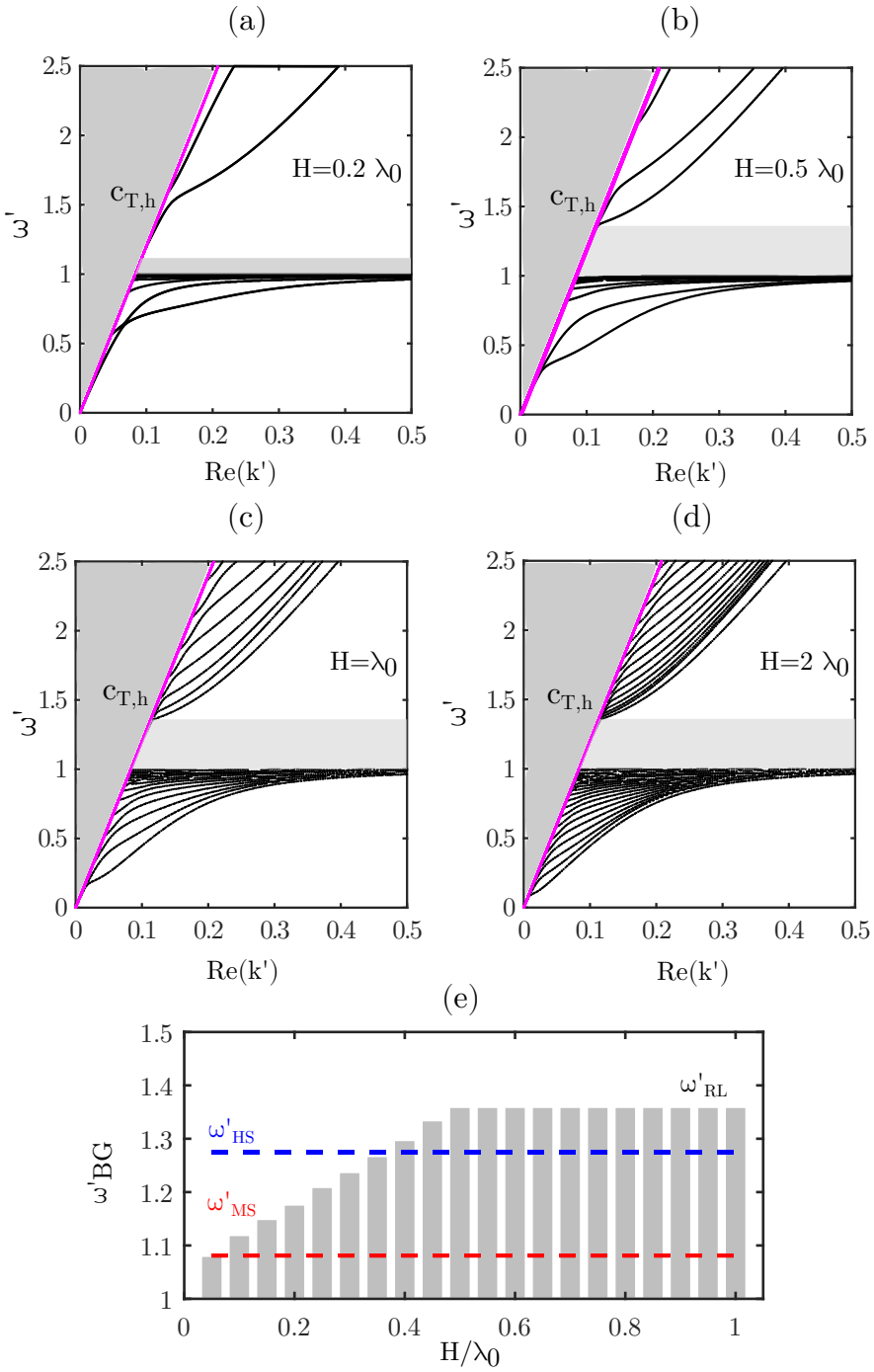

Figure 10: Dispersion curves of real wavenumbers for a semi-infinite resonant medium consisting of a homogeneous half-space below a resonant layer with the depth of (a) $H = 0.2\lambda_0$, (b) $H = 0.5\lambda_0$, (c) $H = \lambda_0$, and (d) $H = 2\lambda_0$, respectively. (e) Band gap width in normalized angular frequency vs. normalized depth of the resonant layer. The dashed blue line indicates the BG upper edge of a resonant half-space, while the dashed red line indicates the upper edge for a metasurface.

The FE model depicted in Fig. 11c consists of a strip of resonators with depth H placed on top of a homogeneous soil. Following the procedure described for the derivation of the numerical dispersion of the resonant half-space (Sec. 2), the numerical eigensolutions (marked by dots) are calculated and overimposed to the analytical dispersion curves for the two scenarios of thin ($H = 0.2\lambda_0$) and thick ($H = \lambda_0$) resonant layer in Fig. 11a and b, respectively. Among all the numerical eigenmodes, surface solutions, highlighted by blue dots, are selected using the identification criterion reported in Eq. (30). We note that the numerical model also accounts for multiple rotational modes of the resonators as previously seen in the case of resonant half-space (see Fig. 8b), which results in an additional flat branch around $\omega^{'} = 1.72$.

It is evident that numerical and analytical results are in good agreement. In particular, numerical simulations confirm the same variation of the BG width with respect to the resonant layer thickness found analytically. Additionally, an insight on the dispersive properties of the fundamental surface mode confirms its "leaky" behavior within the sound-cone domain, evident by visualizing the full wave field of the mode at $k^{'} = 0.08$

and $\omega^{'} = 1.33$, as shown in Fig. 11d. The same mode remains instead confined to the surface when computed outside the sound-cone region (see Fig. 11e).

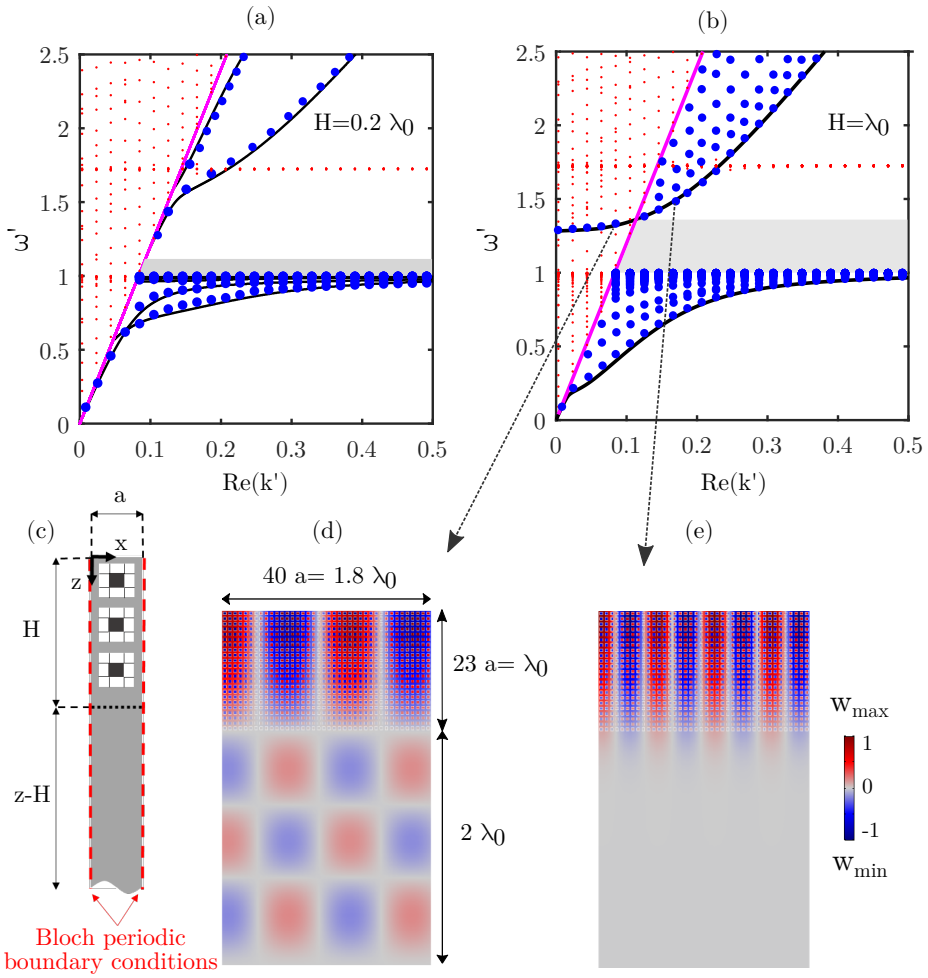

Figure 11: (a) FE surface modes (blue dots), discriminated according to the criterion reported in Eq. (30), and over-imposed to the analytical dispersion relation (solid lines) for $H = 0.2\lambda_0$ and (b) $H = \lambda_0$. (c) A representative unit cell of a resonant barrier on top of a homogeneous soil. (d) The vertical displacement wave field of a leaky surface mode corresponding to $k^{'} = 0.08$ and $\omega^{'} = 1.33$. (e) The vertical displacement wave field of the fundamental surface mode for $k^{'} = 0.18$ and $\omega^{'} = 1.54$. Note that the resonators move out-of-phase with respect to the host medium.

4. Surface waves transmission through a finite-length seismic barrier

Finally, we investigate the propagation of surface waves within a domain composed by a resonant barrier of finite dimensions embedded within a homogeneous non-resonant half-space. Our aim is twofold: first, we want to verify the accuracy of the effective medium description for harmonic analyses; second, we want to evaluate the attenuation properties of the finite length resonant barrier. To this end, we develop two dedicated finite element models: the first model accounts for the true geometry and materials of the barrier, the second, instead, utilizes an effective resonant medium to replace the barrier. In both the models, the domain of interest $L_t \times H_t$, depicted in Fig. 12a, has dimensions of $10\lambda_0 \times 3\lambda_0$, respectively. The barrier is located at a distance of $5\lambda_0$ from the input source, with a length of $2\lambda_0$ and a variable depth H. A vertical unitary displacement, applied at a distance $d_s = \lambda_0$ from the domain edge, is used as a point source to generate surface waves. An output region of length $L_{out} = 2\lambda_0$ is used to recover the signal amplitude after the resonant portion. Low reflecting boundary conditions (LRBCs) are applied at the lateral and bottom edges to reduce wave reflections. Both the domains are discretized by Lagrange quadrilateral elements with a minimum and maximum mesh dimension of $d_{min} = a/10$ and $d_{max} = \lambda_0/5$, respectively.

Frequency-domain analyses are performed within the range of $\omega' = [0.7, 2.5]$ for a resonant layer of thickness $H = \lambda_0$. We define a transmission coefficient calculated as [53]:

$$T(\omega') = \frac{\int_0^{L_{out}} |w_r| dx}{\int_0^{L_{out}} |w_p| dx} \tag{33}$$

where w_r is the vertical nodal displacement as calculated from the FE simulations along the output domain, while w_p is the vertical nodal displacement calculated within the same domain using a twin reference model where the resonant domain is substituted by the homogeneous non-resonant material $(c_{T,h}, c_{L,h}, \rho_h)$.

The true barrier model and the effective resonant layer provide analogous values of the transmission coefficient within the whole frequency range of interest (see Fig. 12b). Similarly, the vertical displacement wave fields obtained by means of the two FE models (true barrier and effective layer) are in excellent agreement for harmonic analyses within and outside the band gap region (see Fig. 13a,b for harmonic simulations at $\omega' = 1$ and Fig. 13c,d for harmonic simulations at $\omega' = 1.3$). In accordance with the prediction of the dispersion curve in Fig. 11b, the surface wave propagation is hindered through the resonant layer for a harmonic excitation within the BG range (see Fig. 13b). In addition, Fig. 13d highlights the attenuation of a leaky surface mode, which spreads part of its elastic energy below the barrier.

These results confirm the possibility of using the effective model within a FE approach. Thus, we perform a parametric study and calculate the transmission coefficients of resonant layers with thickness $H = [0.2, 0.5, 1]\lambda_0$. The results are displayed in Fig. 14 and prove that the barrier attenuation frequency range varies with the barrier depth, as predicted by the proposed dispersion laws. Similarly, the attenuation efficiency of the resonant layer increases with an increase of the barrier depth. For all the cases, the attenuation peaks are located in the frequency range close to the metamaterial resonance, where the EMD assumes large negative values. Within this frequency range, a negligible part of the energy is transmitted in the form of surface solutions traveling below the resonant layer (see Fig. 13a). Conversely, the transmission coefficients assume larger values outside the negative EMD region, since surface waves are attenuated only due to energy leakage. Attenuation due to leakage is indeed much less effective than attenuation due to negative EMD (see Fig. 14) and would require a much longer barrier to significantly reduce the surface wave amplitude.

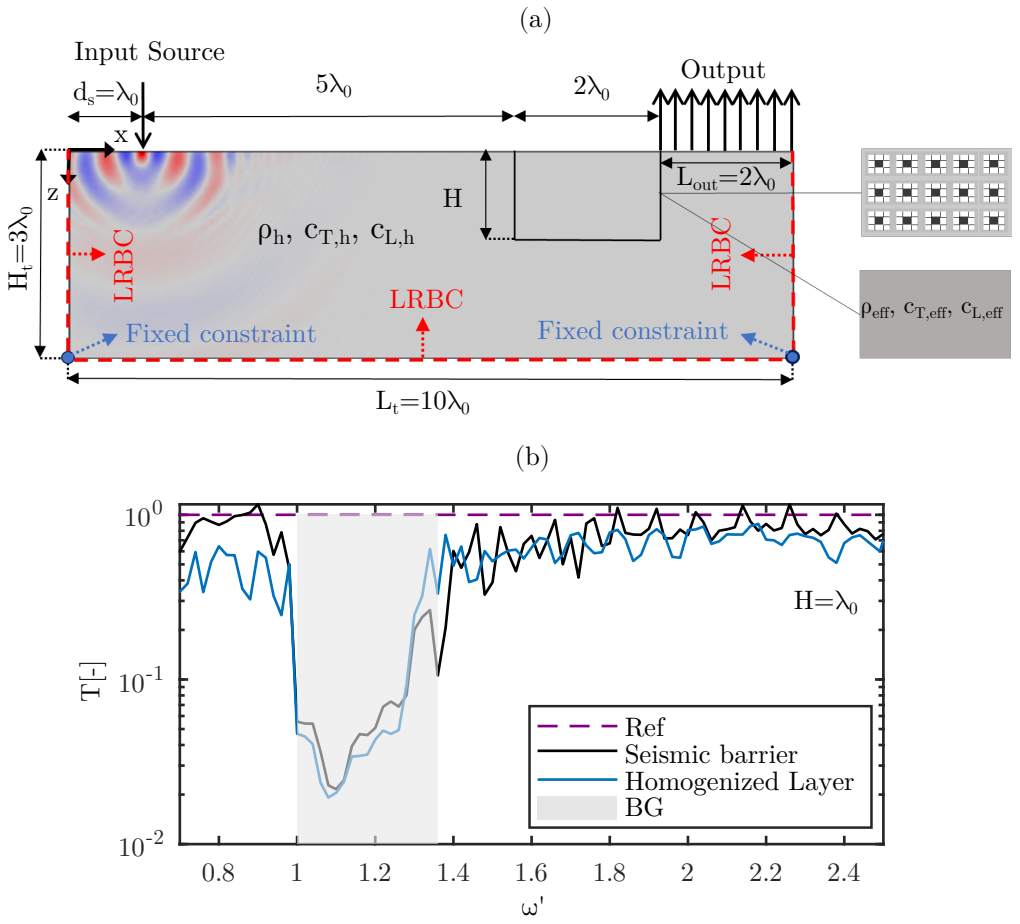

Figure 12: (a) Schematic of the FE model used for the calculation of the transmission coefficients. (b) Comparison of transmission coefficients $T(\omega')$ calculated for the seismic barrier and homogenized layer with an identical depth of $H = \lambda_0$.

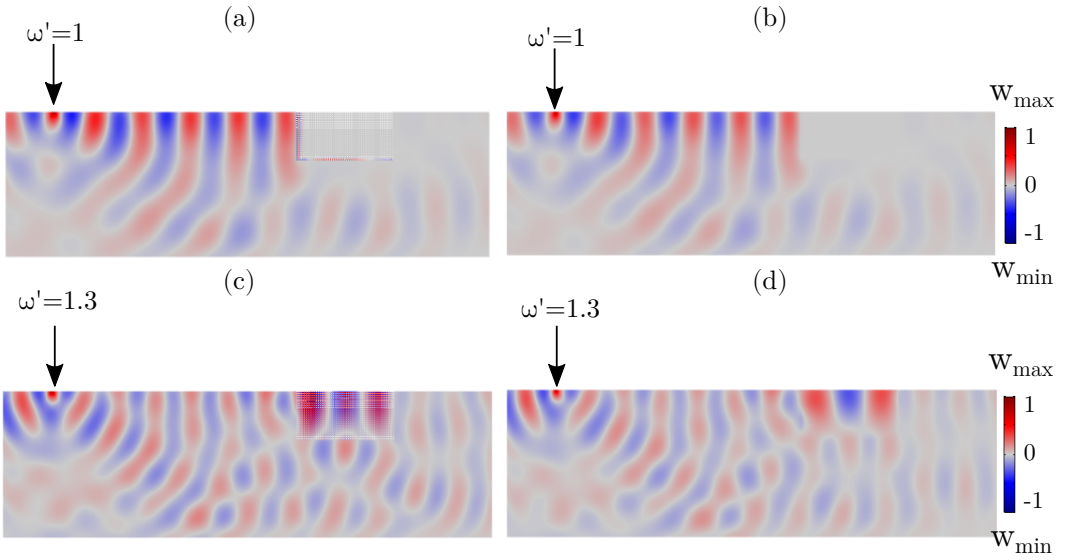

Figure 13: Snapshots of the vertical displacement field (z-axis) for (a) the seismic barrier and (b) its equivalent resonant layer driven by a vertical harmonic excitation at $\omega^{'} = 1$ and for (c) the seismic barrier (d) and (d) its equivalent resonant layer driven by a vertical harmonic excitation at $\omega^{'} = 1.3$.

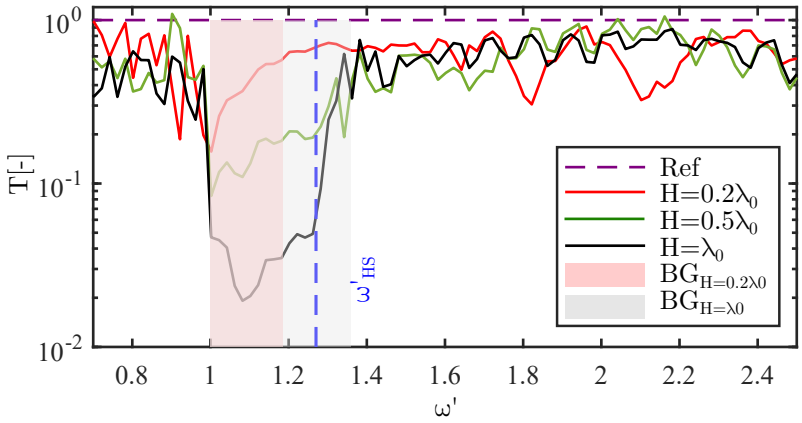

Figure 14: Transmission coefficients of resonant layers with different thicknesses, $H = [0.2, 0.5, 1]\lambda_0$. The red box highlights the band gap of $H = 0.2\lambda_0$, while the shaded gray region marks the band gap of $H = 0.5\lambda_0$ and $H = \lambda_0$. (c)

5. Conclusions

In this work we have proposed an original dispersion relation for vertically polarized surface waves in resonant metamaterials. The metamaterial is modeled via a simple but rather effective homogenization approach, that holds in long-wavelength regime, and yields an equivalent homogeneous material with proper effective elastic parameters (longitudinal and shear bulk modulus) and density.

The developed formulation can handle the case of a fully resonant half-space, the case of finite-thickness resonant layer over a non resonant half space as well as the scenario of a thin resonant layer, also known as metasurface. According to our model, in the fully resonant half-space a band gap in the spectrum of surface waves of the Rayleigh-type opens in the frequency region where the phase speeds of the bulk waves become imaginary.

To discuss the capabilities of our formulation, we have investigated the dynamics of a seismic barrier of meter-size resonators, modelled as a resonant layer of finite thickness. We have shown that a resonant layer of finite thickness H supports the propagation of multiple surface waves. Still, these multiple modes get hybridized by the localized resonances of the inclusions leading to the emergence of a low-frequency band gap. We have proven that the band gap width is related to the thickness of the resonant layer, and we have shown that for thicknesses $H > 0.4/\lambda_0$, the width of the band gap is larger than the one of the full resonant half space. This unexpected result is due to the existence of a leaky surface mode with phase velocity higher than the shear velocity of the host material in a narrow frequency region above the bulk band gap. All these observations have been confirmed via numerical simulations, both in terms of dispersion properties and transmission coefficients. We recognize the

preliminary nature of the results discussed in this case study which discards some of the complexities typically found in real soil, namely a more complex stratigraphy, the presence of a variable water table, as well as material non-linearities. However, these additional complexities are generally neglected (in the long wavelength, low amplitude wave regime) to allow for the development of analytical formulations able to describe the fundamental dynamics of the seismic problem. Overall, our approach provides the required analytical framework to extend current studies on metasurfaces in different domains of applications by accounting for the effective depth of the resonant layer.

Acknowledgments

We acknowledge support by the project "Seismology and Earthquake Engineering Research Infrastructure Alliance for Europe (SERA)". This project has received funding from the European Union's Horizon 2020 research and innovation programme under grant agreement No.730900. A.P. acknowledges the support of the University of Bologna - DICAM through the research fellowship "Metamaterials for seismic waves attenuation".

Conflict of interest

The authors declare that they have no conflict of interest.

Appendix A. A single-resonator barrier modeled as a locally resonant metasurface

The dynamics of a resonant layer with a very thin depth, for example, the case of a barrier with one unit cell ($H = a$), can be adequately described as a resonant metasurface (see Fig. A.15a), an array of subwavelength mass-spring resonators attached to the free surface of a homogeneous elastic half-space. Such a configuration can be analysed by modelling the presence of the resonator as a stress distribution applied on the free surface of the half-space [54]. According to this description, the dispersion relation of the resonant metasurface interacting with vertically polarized surface waves reads [38]:

$$\left(\left(\frac{\omega}{\omega_r}\right)^2 - 1\right)\left[\left(2 - \left(\frac{\omega}{k\, c_{T,h}}\right)^2\right)^2 - 4\sqrt{1 - \left(\frac{\omega}{k\, c_{L,h}}\right)^2}\sqrt{1 - \left(\frac{\omega}{k\, c_{T,h}}\right)^2}\right] = \frac{m_{res}\,\omega^4}{A\,\rho_h\, c_{T,h}^4\, k^3}\sqrt{1 - \left(\frac{\omega}{k\, c_{L,h}}\right)^2} \tag{A.1}$$

where $A = a_r t$ is an average area where each resonator exerts its stress. In Fig. A.15b, we compare the dispersive properties of a single layer $H = a$ resonant barrier modelled according to the metasurface description (Eq. (A.1), red dashed lines in Fig. A.15b) and the framework proposed in our work (Eq. (24), black lines in Fig. A.15b).

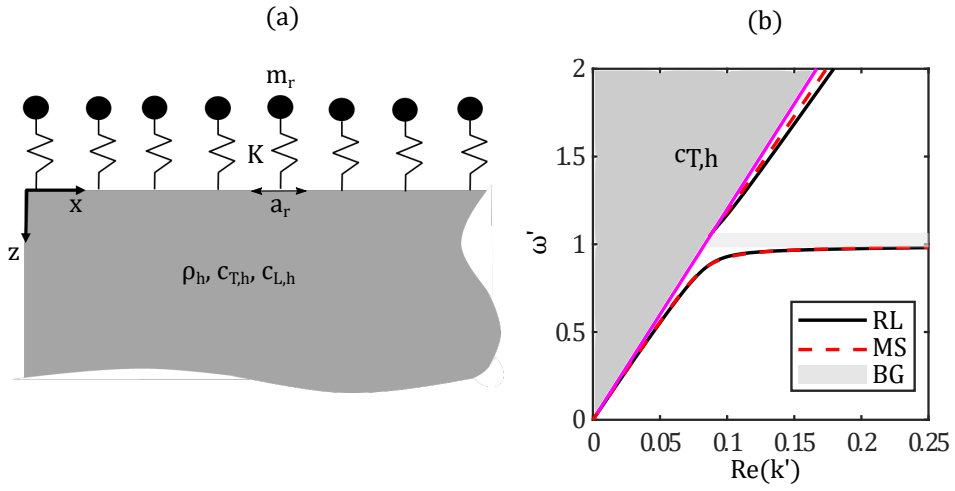

Figure A.15: (a) Schematic of the metasurface layer attached to the free surface of a homogeneous half-space. (b) Dispersion of the resonant layer composed of a single unit cell embedded to the host material (RL) vs. locally resonant metasurface (MS).

It is evident that the two models provide analogous results in the case of a thin resonant layer.

References

[1] V. G. Veselago, The electrodynamics of substances with simultaneously negative values of ϵ and μ, Phys. Usp. 10 (1968) 509–514.

[2] J. B. Pendry, Negative refraction makes a perfect lens, Phys. Rev. Lett. 85 (2000) 3966–3969.

[3] M. Kadic, T. Bückmann, R. Schittny, M. Wegener, Metamaterials beyond electromagnetism, Reports on Progress in Physics 76 (2013) 126501.

[4] G. Ma, P. Sheng, Acoustic metamaterials: From local resonances to broad horizons, Science Advances 2 (2016).

[5] Z. Liu, X. Zhang, Y. Mao, Y. Y. Zhu, Z. Yang, C. T. Chan, P. Sheng, Locally resonant sonic materials, Science 289 (2000) 1734–1736.

[6] Z. Liu, C. T. Chan, P. Sheng, Three-component elastic wave band-gap material, Phys. Rev. B 65 (2002) 165116.

[7] G. W. Milton, J. R. Willis, On modifications of newton's second law and linear continuum elastodynamics, Proceedings of the Royal Society A: Mathematical, Physical and Engineering Sciences 463 (2007) 855–880.

[8] H. H. Huang, C. T. Sun, Anomalous wave propagation in a one-dimensional acoustic metamaterial having simultaneously negative mass density and young's modulus, The Journal of the Acoustical Society of America 132 (2012) 2887–2895.

[9] H. Huang, C. Sun, G. Huang, On the negative effective mass density in acoustic metamaterials, International Journal of Engineering Science 47 (2009) 610 – 617.

[10] Y. Xiao, J. Wen, X. Wen, Longitudinal wave band gaps in metamaterial-based elastic rods containing multi-degree-of-freedom resonators, New Journal of Physics 14 (2012) 033042.

[11] M. Nouh, O. Aldraihem, A. Baz, Vibration Characteristics of Metamaterial Beams With Periodic Local Resonances, Journal of Vibration and Acoustics 136 (2014) VIB–13–1435.

[12] P. F. Pai, H. Peng, S. Jiang, Acoustic metamaterial beams based on multi-frequency vibration absorbers, International Journal of Mechanical Sciences 79 (2014) 195 – 205.

[13] H. B. A. Ba'ba'a, M. Nouh, Mechanics of longitudinal and flexural locally resonant elastic metamaterials using a structural power flow approach, International Journal of Mechanical Sciences 122 (2017) 341 – 354.

[14] Y. Lai, Y. Wu, P. Sheng, Z.-Q. Zhang, Hybrid elastic solids, Nat Mater 10 (2011) 620–624.

[15] A. Sridhar, L. Liu, V. Kouznetsova, M. Geers, Homogenized enriched continuum analysis of acoustic metamaterials with negative stiffness and double negative effects, Journal of the Mechanics and Physics of Solids 119 (2018) 104 – 117.

[16] C. Gao, D. Halim, X. Yi, Study of bandgap property of a bilayer membrane-type metamaterial applied on a thin plate, International Journal of Mechanical Sciences 184 (2020) 105708.

[17] Z. Li, H. Hu, X. Wang, A new two-dimensional elastic metamaterial system with multiple local resonances, International Journal of Mechanical Sciences 149 (2018) 273 – 284.

[18] E. Baravelli, M. Ruzzene, Internally resonating lattices for bandgap generation and low-frequency vibration control, Journal of Sound and Vibration 332 (2013) 6562 – 6579.

[19] A. Bacigalupo, L. Gambarotta, Simplified modelling of chiral lattice materials with local resonators, International Journal of Solids and Structures 83 (2016) 126–141.

[20] K. H. Matlack, A. Bauhofer, S. Krödel, A. Palermo, C. Daraio, Composite 3D-printed meta-structures for low frequency and broadband vibration absorption, Proceedings of the National Academy of Sciences of the United States of America 113 (2015).

[21] W. Jiang, M. Yin, Q. Liao, L. Xie, G. Yin, Three-dimensional single-phase elastic metamaterial for low-frequency and broadband vibration mitigation, International Journal of Mechanical Sciences 190 (2021) 106023.

[22] M. I. Hussein, M. J. Frazier, Metadamping: An emergent phenomenon in dissipative metamaterials, Journal of Sound and Vibration 332 (2013) 4767 – 4774.

[23] M. Lewińska, V. Kouznetsova, J. Van Dommelen, A. Krushynska, M. Geers, The attenuation performance of locally resonant acoustic metamaterials based on generalised viscoelastic modelling, International Journal of Solids and Structures 126 (2017) 163–174.

[24] A. Aladwani, M. Nouh, Mechanics of metadamping in flexural dissipative metamaterials: Analysis and design in frequency and time domains, International Journal of Mechanical Sciences 173 (2020) 105459.

[25] F. Vadalá, A. Bacigalupo, M. Lepidi, L. Gambarotta, Free and forced wave propagation in beam lattice metamaterials with viscoelastic resonators, International Journal of Mechanical Sciences (2020) 106129.

[26] L. Bonanomi, G. Theocharis, C. Daraio, Wave propagation in granular chains with local resonances, Physical Review E 91 (2015) 033208.

[27] A. Casalotti, S. El-Borgi, W. Lacarbonara, Metamaterial beam with embedded nonlinear vibration absorbers, International Journal of Non-Linear Mechanics 98 (2018) 32–42.

[28] W. Jiao, S. Gonella, Intermodal and subwavelength energy trapping in nonlinear metamaterial waveguides, Physical Review Applied 10 (2018) 024006.

[29] M. Miniaci, A. Krushynska, A. S. Gliozzi, N. Kherraz, F. Bosia, N. M. Pugno, Design and fabrication of bioinspired hierarchical dissipative elastic metamaterials, Phys. Rev. Applied 10 (2018) 024012.

[30] X. Xu, M. V. Barnhart, X. Li, Y. Chen, G. Huang, Tailoring vibration suppression bands with hierarchical metamaterials containing local resonators, Journal of Sound and Vibration 442 (2019) 237 – 248.

[31] Y. Chen, X. Li, H. Nassar, A. N. Norris, C. Daraio, G. Huang, Nonreciprocal wave propagation in a continuum-based metamaterial with space-time modulated resonators, Physical Review Applied 11 (2019) 064052.

[32] M. Attarzadeh, J. Callanan, M. Nouh, Experimental observation of nonreciprocal waves in a resonant metamaterial beam, Physical Review Applied 13 (2020) 021001.

[33] J. Marconi, E. Riva, M. Di Ronco, G. Cazzulani, F. Braghin, M. Ruzzene, Experimental observation of nonreciprocal band gaps in a space-time-modulated beam using a shunted piezoelectric array, Physical Review Applied 13 (2020) 031001.

[34] M. Addouche, M. A. Al-Lethawe, A. Elayouch, A. Khelif, Subwavelength waveguiding of surface phonons in pillars-based phononic crystal, AIP Advances 4 (2014) 124303.

[35] M. Al Lethawe, M. Addouche, S. Benchabane, V. Laude, A. Khelif, Guidance of surface elastic waves along a linear chain of pillars, AIP Advances 6 (2016) 121708.

[36] D. Colquitt, A. Colombi, R. Craster, P. Roux, S. Guenneau, Seismic metasurfaces: Sub-wavelength resonators and rayleigh wave interaction, Journal of the Mechanics and Physics of Solids 99 (2017) 379 – 393.

[37] A. Palermo, S. Krödel, A. Marzani, C. Daraio, Engineered metabarrier as shield from seismic surface waves, Scientific Reports 6 (2016) 39356.

[38] N. Boechler, J. K. Eliason, A. Kumar, A. A. Maznev, K. A. Nelson, N. Fang, Interaction of a contact resonance of microspheres with surface acoustic waves, Phys. Rev. Lett. 111 (2013) 036103.

[39] A. Colombi, P. Roux, S. Guenneau, P. Gueguen, R. V. Craster, Forests as a natural seismic metamaterial: Rayleigh wave bandgaps induced by local resonances, Scientific reports 6 (2016) 19238.

[40] X. Pu, A. Palermo, Z. Cheng, Z. Shi, A. Marzani, Seismic metasurfaces on porous layered media: Surface resonators and fluid-solid interaction effects on the propagation of rayleigh waves, International Journal of Engineering Science 154 (2020) 103347.
[41] A. A. Maznev, V. E. Gusev, Waveguiding by a locally resonant metasurface, Phys. Rev. B 92 (2015) 115422.
[42] A. Colombi, S. Guenneau, P. Roux, R. V. Craster, Transformation seismology: composite soil lenses for steering surface elastic rayleigh waves, Scientific reports 6 (2016) 25320.
[43] A. Palermo, A. Marzani, Control of love waves by resonant metasurfaces, Scientific Reports 8 (2018) 7234.
[44] A. Colombi, D. J. Colquitt, P. P. Roux, S. Guenneau, R. V. Craster, A seismic metamaterial: The resonant metawedge, Scientific reports 6 (2016) 27717.
[45] A. Palermo, Y. Wang, P. Celli, C. Daraio, Tuning of surface-acoustic-wave dispersion via magnetically modulated contact resonances, Physical Review Applied 11 (2019) 044057.
[46] A. Palermo, P. Celli, B. Yousefzadeh, C. Daraio, A. Marzani, Surface wave non-reciprocity via time-modulated metamaterials, Journal of the Mechanics and Physics of Solids (2020) 104181.
[47] Z. Cheng, Z. Shi, Composite periodic foundation and its application for seismic isolation, Earthquake Engineering & Structural Dynamics 47 (2018) 925–944.
[48] F. Basone, M. Wenzel, O. S. Bursi, M. Fossetti, Finite locally resonant metafoundations for the seismic protection of fuel storage tanks, Earthquake Engineering & Structural Dynamics 48 (2019) 232–252.
[49] A. S. Phani, J. Woodhouse, N. A. Fleck, Wave propagation in two-dimensional periodic lattices, The Journal of the Acoustical Society of America 119 (2006) 1995–2005.
[50] A. A. Maznev, Bifurcation of avoided crossing at an exceptional point in the dispersion of sound and light in locally resonant media, Journal of Applied Physics 123 (2018) 091715.
[51] K. F. Graff, Wave motion in elastic solids, Dover books on physics, Dover, New York, NY, 1991.
[52] COMSOL Multiphysics®, Comsol ab, stockholm, sweden., 2020.
[53] A. Palermo, M. Vitali, A. Marzani, Metabarriers with multi-mass locally resonating units for broad band rayleigh waves attenuation, Soil Dynamics and Earthquake Engineering 113 (2018) 265 – 277.
[54] E. A. Garova, A. A. Maradudin, A. P. Mayer, Interaction of rayleigh waves with randomly distributed oscillators on the surface, Phys. Rev. B 59 (1999) 13291–13296.